Bajo and Yurimoto
Journal of Analytical Science and Technology (2024) 15:19
https://doi.org/10.1186/s40543-024-00429-1

Journal of Analytical Science and Technology

REVIEW

Open Access

Nanoscale analysis of noble gas in solids

Ken-ichi Bajo[1] and Hisayoshi Yurimoto[1*]

Abstract

Noble gases are useful tracers for geochemistry, used to elucidate the origin and evolution of the solar system and planets. Noble gas analyses have been limited to bulk and spot analyses of solids and have yet to be developed for two- and three-dimensional imaging analysis. Recent developments in He isotope imaging using secondary neutral mass spectrometry are reviewed. The images have been fully quantified, and the spatial resolution has reached the nanoscale. The detection limit has been reduced to the level of ~ 10^{-3} cm^3 STP g^{-1} (~ 10^{17} cm^{-3}, ~ 1 ppma) for helium at lateral micrometer resolution. With this development, the concentration distribution of He in solids has been visualized as a map for the first time.

Keywords Noble gas, Micro analysis, Mass spectrometry, Laser, Tunneling ionization, Liquid ion metal source, Mapping, Isotope, Meteorite

Introduction

Noble gases have been utilized as tracers in geochemistry and cosmochemistry to understand the origin and evolution of natural samples. A special technique, called noble gas mass spectrometry under vacuum static condition, is required to measure noble gases, because of their extremely low abundance in solids and their chemically inert properties. The detection limits of state-of-the-art noble gas mass spectrometry are at ~ 1×10^{-12} cm^3 STP (~ 3×10^7 atoms) for ^{4}He (Heck et al. 2009; Nagao et al. 2011), corresponding to concentrations of 6×10^{-7}, 6×10^{-4}, and 6×10^{-1} cm^3 STP g^{-1} (5×10^{13}, 5×10^{16}, and 5×10^{19} atom cm^{-3}; 0.0005, 0.5, and 500 ppma) for olivine of 100, 10, and 1 μm cubes per side, respectively. Focused laser ablation techniques have been introduced into noble gas mass spectrometry for in situ analyses. The spatial resolution reaches ~ 50 μm for both lateral and depth directions (Nakamura et al. 1999; Okazaki et al. 2001; Sumino et al. 2008). The detection limit of the concentration with laser ablation is calculated to be ~ 2×10^{-6} cm^3 STP g^{-1} (2×10^{14} atom cm^{-3}, 2 ppba) using noble gas mass spectrometry.

Secondary ion mass spectrometry (SIMS) is a powerful in situ technique for the trace element analysis of solids and has been widely applied to noble gas measurements. The detection limits were found to be ~ 0.1 cm^3 STP g^{-1} (~ 10^{19} atom cm^{-3}, 100 ppma) for ^{4}He with a spatial resolution of ~ 20 μm for lateral and ~ 10 nm in depth (Gnaser and Oechsner 1991). The detection limit concentration is calculated to be ~ 1×10^{-12} cm^3 STP (~ 4×10^7 atoms) for ^{4}He under the measurement volume. The absolute detection limit of ^{4}He by SIMS is similar to that of noble gas mass spectrometry although the spatial resolution of SIMS is much higher than that of the laser ablation noble gas mass spectrometry. However, the detection limit concentration is approximately five orders of magnitude higher than that of laser ablation noble gas mass spectrometry. Since ^{4}He concentrations of natural samples are less than 10^{-2} cm^3 STP g^{-1} (~ 10^{18} cm^{-3}) (Bogard and Johnson 1983; Obase et al. 2021), SIMS measurement capabilities are insufficient for natural sample analyses mainly due to the low secondary ion yields (number ratio of ionized atom to sputtered atom) for noble gases. Therefore, the ionization efficiency of noble gases should be enhanced to realize micrometer-scale lateral resolution for noble gas analyses.

*Correspondence:
Hisayoshi Yurimoto
yuri@ep.sci.hokudai.ac.jp
[1] Natural History Sciences, IIL, Hokkaido University, Sapporo 001-0021, Japan

We have applied strong-field ionization to noble gases in secondary neutral mass spectrometry (SNMS) (Ebata et al. 2012). The detection limits were at ~ 0.06 cm^3 STP g^{-1} (~ 5×10^{18} cm^{-3}, 50 ppma) for ^{4}He with a spatial resolution of ~ 3 μm for lateral and ~ 10 nm for depth (Bajo et al. 2015). The detection limits have recently been improved to ~ 3×10^{-3} cm^3 STP g^{-1} (3×10^{17} cm^{-3}, 3 ppma) for ^{4}He with the same spatial resolution. The detection limit concentration is calculated to be ~ 4×10^{-14} cm^3 STP (~ 1×10^6 atoms) for ^{4}He atom detection from the measurement volume. This is nearly two orders of magnitude better than the detection limit of noble gas mass spectrometry, and the lateral resolution is more than one order of magnitude better than that of noble gas mass spectrometry. In this paper, we discuss the recent developments in our SNMS studies and some applications of cosmochemical materials.

Instrumental configuration of laser ionization mass nanoscope (LIMAS)

The SNMS instrument used in this study is a laser ionization mass nanoscope (LIMAS) at Hokkaido University (Ebata et al. 2012) (Fig. 1). LIMAS is equipped with a Ga liquid metal ion source (Ga-LMIS), a femtosecond (fs) laser, and a multi-turn time-of-flight mass spectrometer (TOF–MS). The Ga beam generated by the Ga-LMIS is pulsed by an ion blanker. The pulsed beam is irradiated onto the sample surface at an incident angle of 35° to the sample surface. The surface is sputtered by the beam, producing a sputtered plume. The neutrals in the plume are ionized by a pulsed laser beam generated by the fs laser. The ions are then injected into the TOF–MS system to obtain the mass spectrum. The timing of each step is controlled to an accuracy of 5 ns (Bajo et al. 2016). The measurement cycles are typically repeated at 1 kHz.

Nano-sized probe for the primary beam

The smallest measurement area of LIMAS corresponds to the sputtering volume of the primary beam. Therefore, the measurement area is mainly limited by the primary beam diameter in the lateral direction and the primary beam energy in the depth direction. We use the LMIS as the primary ion beam source to obtain a small beam. The LMIS uses Ga, which is heated to the liquid state and used to form an electrospray Taylor cone to produce ions. Ions from the electrospray Taylor cone are produced by field evaporation at the sharp tip of the cone, which has a high electric field. We use monoisotopic ^{69}Ga as the metal source to reduce the energy aberration of the primary beam and to produce a simpler TOF spectrum of the pulsed primary beam.

Spherical and chromatic aberrations limit the ion beam size at a given kinetic energy. The aberrations can be highly reduced by an aberration corrector installed in LIMAS (Bajo et al. 2016; Itose et al. 2011; Nagata et al. 2019). The radial intensity distribution of the LIMAS primary beam consists of Gaussian and halo profiles. Both the profiles are efficiently improved by the aberration corrector. The corrector reduces the diameter of the Gaussian profile by ~ 1/2 (Nagata et al. 2019). The smallest primary beam of LIMAS is ~ 10 nm (the knife-edge method of 16–84% criterion) at a beam current of 3 pA, and the largest is ~ 500 nm at 30 nA (Fig. 2). The highest

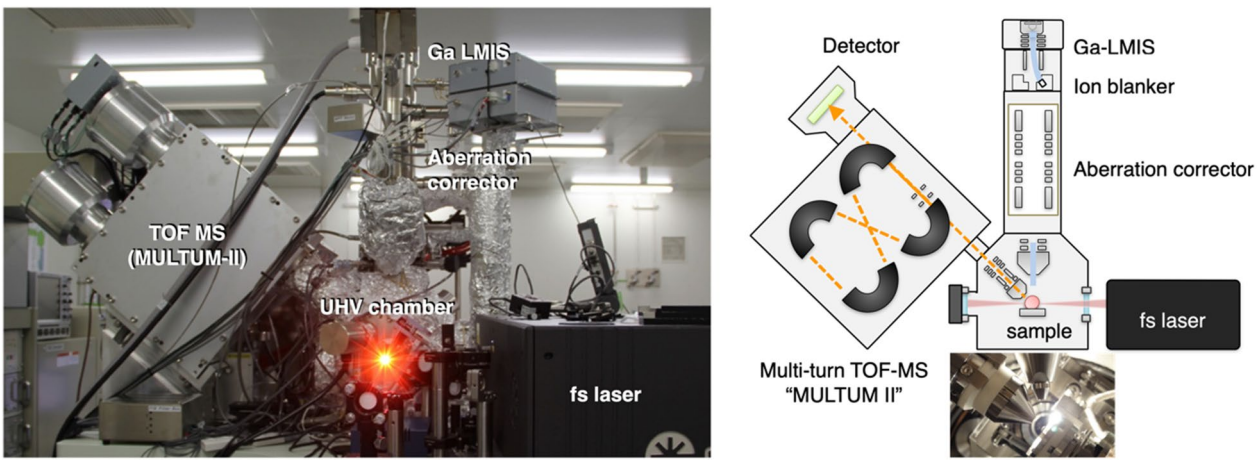

Fig. 1 Photograph and schematic image of LIMAS. Configuration of primary and secondary columns and sample holder is inserted. The primary beam is irradiated onto the sample surface at an incident angle of 35° to the sample surface as shown in the inserted picture. Note that the configuration between the primary beam and the sample in the schematic drawing is not correct

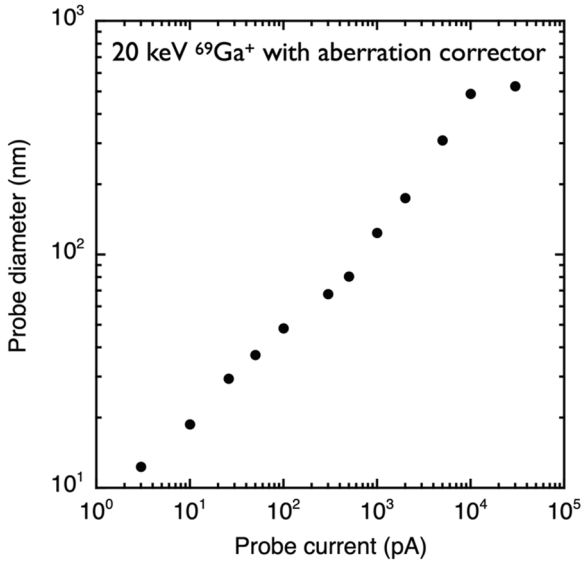

Fig. 2 Relationship between primary beam current and diameter

depth resolution is estimated to be approximately 5 nm, taking into account the impact mixing depth of the sample atoms by the 20–30 keV impact energy of the primary beam. Using a 3 pA beam, scanning ion images of LIMAS have a resolution of ~ 10 nm in the *x*–*y*–*z* directions. The spatial resolution of LIMAS is better than that of Cameca NanoSIMS (Malherbe et al. 2016), but not better than that of atom probe tomography (Greer et al. 2020).

Post-ionization by laser beam

Secondary ion yields using Ga primary ions are generally low for all elements compared to the use of O and Cs primary ions commonly used for SIMS. However, the low secondary ion yields are advantageous for SNMS because ionization is generated after sputtering. We used non-resonant ionization to ionize sputtered neutrals to ionize all elements simultaneously to increase ionization efficiency for all elements without discrimination.

The mechanisms of non-resonant ionization of gas depend on the laser power density (Ivanov et al. 2005; Protopapas et al. 1997). At laser power densities lower than ~ 10^{18} W m^{-2}, the ionization is dominated by multiphoton processes (Fig. 3). As the laser power density increases, the atomic potential is more strongly affected by the laser field, and the potential is distorted to create a sufficient finite barrier. Thus, tunneling ionization becomes dominant. At even higher laser power densities, the potential barrier is completely suppressed and the electrons are free to escape. This is over the barrier ionization.

Mibuka et al. (2008) measured the ionization characteristics of Si, Au, Cu, Fe, Mg, Al, Pt, Pd, Ag, and C in terms of laser power density using LIMAS. The saturation of ionization was experimentally confirmed for all elements. Except for C, the signals are saturated above the laser power density of approximately 2×10^{17} W m^{-2} for the metal elements. The C signals are saturated above ~ 6×10^{17} W m^{-2} owing to the large ionization energy. As the ionization energies of He and Ne are much higher than those of the other elements, the signal saturation occurs above ~ 10^{19} W m^{-2}, while the signals of He still increase with increasing laser power density (Fig. 4) (Ebata et al. 2012). The ionization yield (number ratio of ionized atom to atom in the laser beam) of He reaches ~ 70% at a laser power of 10^{20} W m^{-2} (Yurimoto et al. 2016). The saturation characteristics of most elements, including noble gases, at high laser power densities, suggest that ionization is generated by a strong-field ionization mechanism. Therefore,

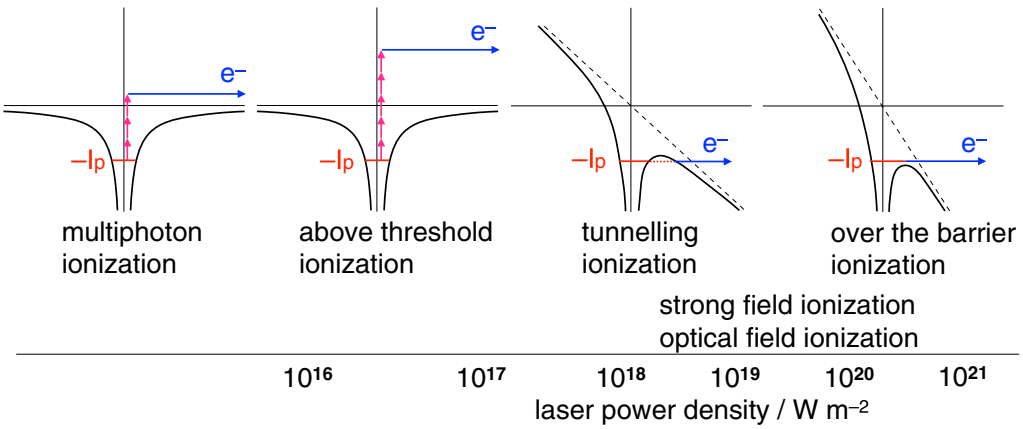

Fig. 3 Schematic diagram showing the possible mechanisms for ionization with superposition of laser field and Coulomb potential for different laser intensities. The laser power densities roughly indicate when each mechanism becomes dominant. Adapted from Protopapas et al. (1997)

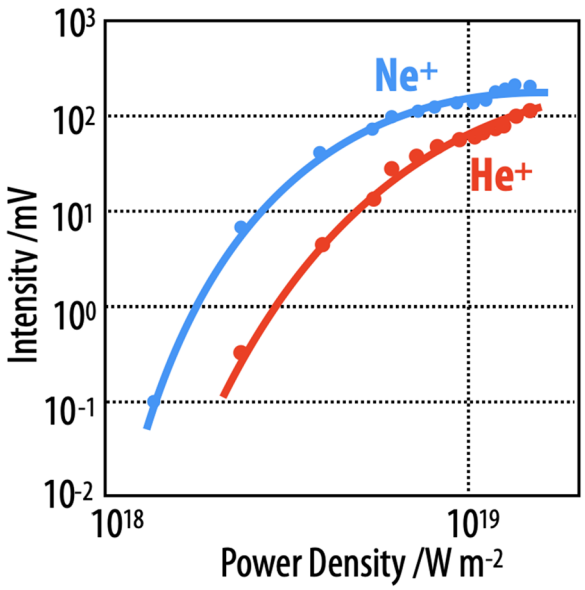

Fig. 4 Laser post-ionization curves of Ne and He as a function of laser power density. Adapted from Ebata et al. (2012)

the matrix effects for quantitative analyses can be significantly reduced in LIMAS compared with secondary ion mass spectrometry (Ebata et al. 2013).

Multi-turn TOF mass spectrometer

A multi-turn TOF mass spectrometer (MULTUM II) (Okumura et al. 2004) is installed in LIMAS. Post-ionized ions are transferred into MULTUM II by an electrostatic lens L1 (Fig. 5). The MULTUM II consist of four electrostatic energy analyzers (EF1–EF4). The ions are injected through a hole in the outer sector electrode of EF4. While the ions are injected into the MULTUM II, the voltage of EF4 is turned off, and turned on again before the ions return. After the ions have passed the desired number of cycles, the voltage of EF1 is turned off to eject the ions from the outer sector electrode of EF1 to the detector. The timing chart of these operations and the configuration of the control hardware are described in detail elsewhere (Bajo et al. 2019; Bajo et al. 2016).

Since the ion optics of the MULTUM II are designed to realize "perfect space and time focusing" conditions (Ishihara et al. 2000), the ion packet in the optics can be principally circumnavigated as many times as desired. The flight path length of the MULTUM II is 1.308 m/cycle. As designed, the TOF peak width of an ion packet of ^{24}Mg is constant at ~ 4 ns (Fig. 6) for any multi-turn cycles. Therefore, the mass-resolving power increases proportionately to the number of multi-turn cycles. The mass-resolving power reaches close to $M/\Delta M = \sim 10^6$ after multi-turn cycles of 1000, corresponding to a flight path length of ~ 1.3 km.

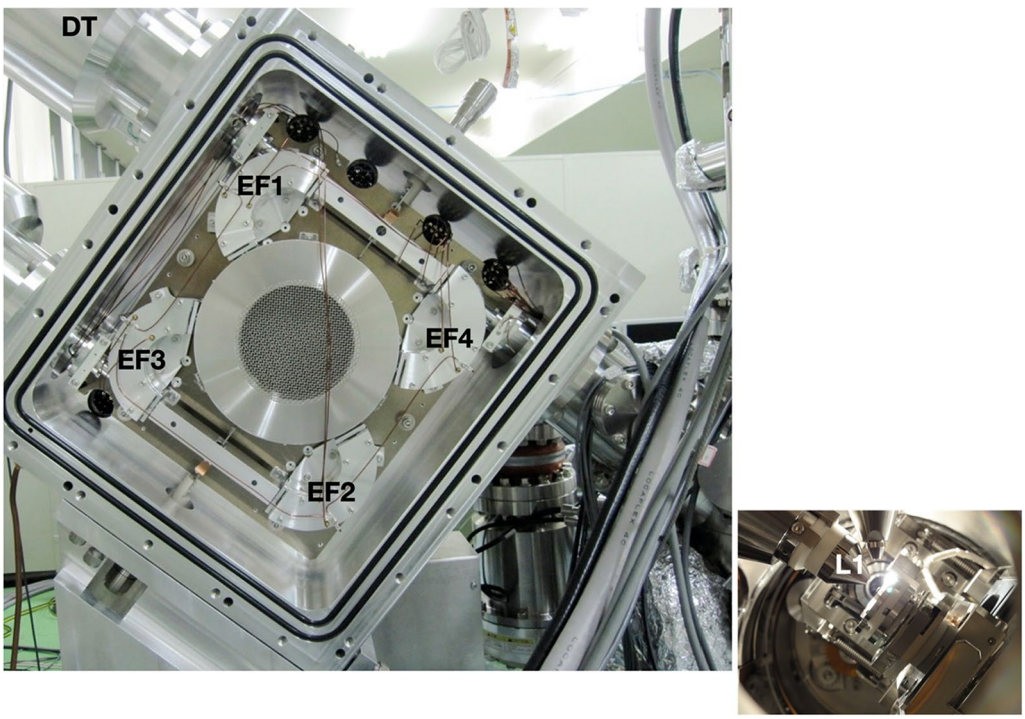

Fig. 5 Photograph of LIMAS interior. *L* lens, *EF* electrostatic energy filter, and *DT* detector

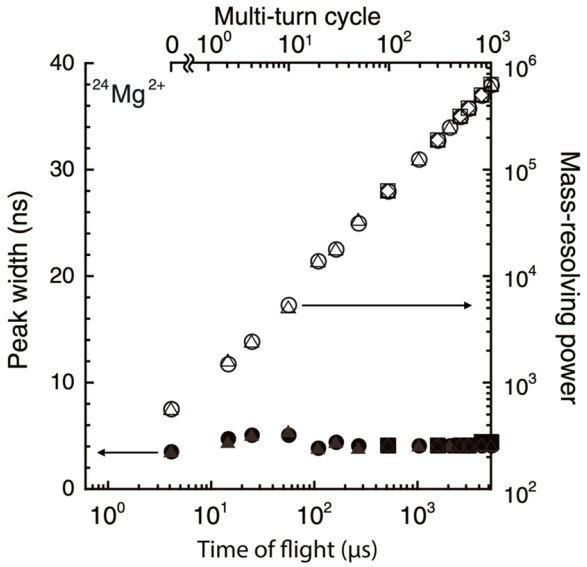

Fig. 6 Relationship between multi-turn cycle, time-of-flight, peak width (solid symbol), and the mass-resolving power (open symbol) for $^{24}Mg^{2+}$ ions. Adapted from Tonotani et al. (2016)

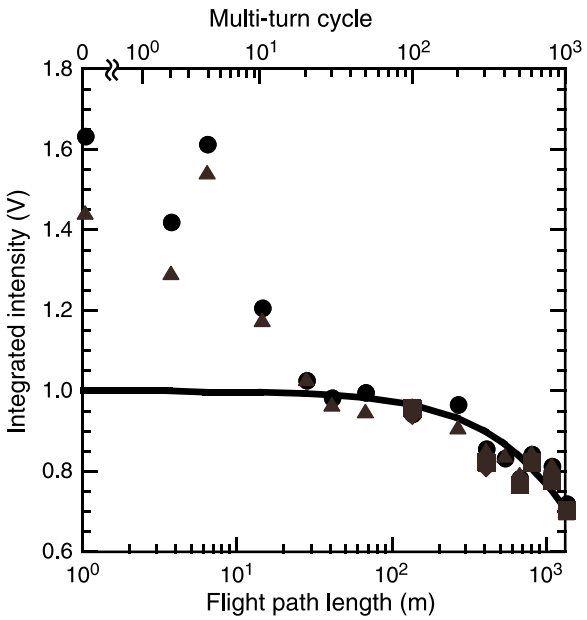

Fig. 7 Ion intensity of $^{24}Mg^{2+}$ as a function of the flight path length. Each symbol corresponds to an independent experiment. The solid curve shows the case where the ion intensity decreases due to collisions with residual gas in the mass spectrometer. Adapted from Tonotani et al. (2016)

The ion transmittance of the MULTUM II decreases with increasing flight pass length (Fig. 7). During the first 20 multi-turn cycles, the ion intensity decreases rapidly to 60–70% of the initial value, after which the rate of the intensity reduction becomes slower. The gradual decrease after the 20 cycles is caused by scattering of the multi-turn ions by collisions with the residual gas in the mass spectrometer (Tonotani et al. 2016). As the intensity decreases rapidly beyond a flight path length of 1 km, the useful mass resolution is limited to ~ 10^6. In order to achieve a higher mass resolution of more than 10^6, a lower pressure of less than 10^{-6} Pa is required in the MULTUM II chamber. A useful yield (number ratio of detected atom to sputtered atom) of ~ 10^{-3} is achieved for Si at $M/\Delta M = \sim 10^6$.

Data acquisition system

The LIMAS data acquisition system is designed for high-speed data acquisition, high-speed data processing, and high-speed data streaming by controlling the timing clocks for LIMAS operation. Mass-separated ions are introduced into the two-stage microchannel plates. The system detects one ion with a signal pulse width of 1.3 ns (Bajo et al. 2019). The pulse heights of the single ion signals are distributed as a Gaussian-like function with 100 ± 60 mV (3σ) (Fig. 8). The tailing toward a higher signal height is because of the simultaneous incidence of ions into the detector. As the Gaussian curve intersects the noise line at ~ 40 mV, an ion signal above 40 mV is noise-free and accounts for more than 99.7% of the detected ions. The ion signals above 40 mV are called discriminated signals.

The discriminated signals are separated by a distributor and counted simultaneously in digital and analog mode. The number of discriminated signal pulses is directly

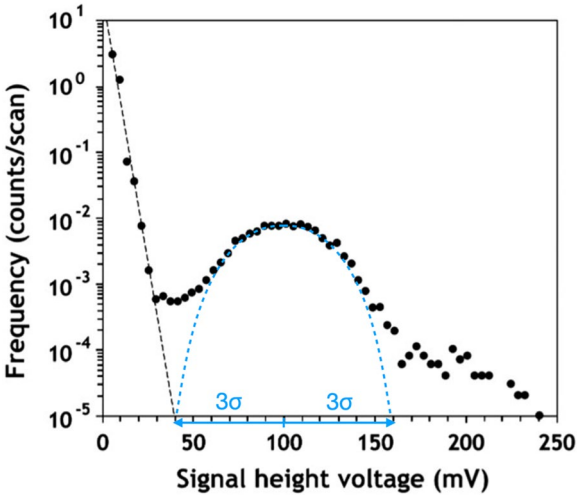

Fig. 8 Pulse height distribution of $^{24}Mg^{2+}$ ions. Black and blue dotted lines represent the least square fit to the data points of the noise and ion signals, respectively. Adapted from Bajo et al. (2019)

counted in digital mode. Contrarily, in analog mode, the accumulated discriminated signal currents are divided by the mean discriminated signal current to derive the ion counts. The saturation phenomenon of the signal acquisition system can be evaluated by measuring the isotope abundance of an element.

We used Mg isotopes to evaluate the saturation phenomenon of the signal acquisition system. Mg has three isotopes with abundances of ^{24}Mg: 0.7899, ^{25}Mg: 0.1000, and ^{26}Mg: 0.1101. Therefore, the major ^{24}Mg ion signals will saturate before the minor Mg isotope signals as the Mg signals from the sample increase. The discriminated signal ratio of ^{25}Mg/^{24}Mg is constant and consistent with the isotope abundance ratio when ^{24}Mg signal intensities are low (Fig. 9). However, as the ^{24}Mg signal intensity increases, the signal ratios also increase. This indicates that a signal saturation of ^{24}Mg occurs. Saturation starts at ~ 0.1 ion/scan in digital mode and ~ 10 ion/scan in analog mode. Readout noise is detected from 10^7 scans in digital mode and 5×10^7 scans in analog mode (Bajo et al. 2019). Therefore, the dynamic range is wider in analog mode, reaching approximately 10^9.

Figure 10 shows the TOF mass spectrum for $m/z=4$ of diamond-like carbon on silicon substrate. The $^{12}C^{3+}$ peak resembles a log-normal distribution (302.73 μs < TOF < 302.80 μs), with a long tail to the right (302.80 μs < TOF). The log-normal distribution is composed of real $^{12}C^{3+}$ signals. However, the tail is a signal of dark currents in the microchannel plates induced by high intensity signals of $^{12}C^{3+}$. If the log-normal distribution could be reduced by the ion gates of MULTUM II (Bajo et al. 2016), the dark currents would disappear. Indeed, no dark currents are detected when the ion gates are operated (Fig. 10). Consequently, an interference-free unperturbed $^4He^+$ peak is detected. The $^4He^+$ peak is generated from the residual He gas in the ultra-high vacuum sample chamber, and its intensity corresponds to a concentration of 3×10^{17} cm^{-3} in solids. The intensity of the signals from the residual gas determines the background signal of LIMAS, and the statistical variation determines the detection limit.

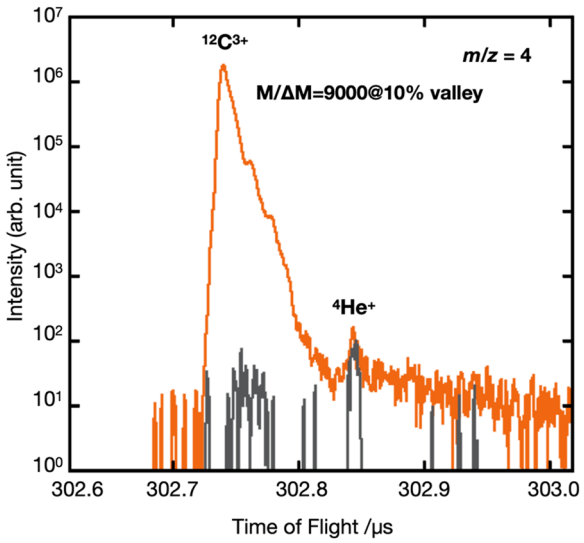

Fig. 10 Mass spectrum of $m/z=4$ from diamond-like carbon substrate. The matrix ion of $^{12}C^{3+}$ and residual gas in the vacuum of $^4He^+$ appeared (orange color line). Ion gates of LIMAS deflect $^2C^{3+}$ ions from the multi-turn trajectory to reduce the intensity without affecting the $^4He^+$ intensity (gray color line)

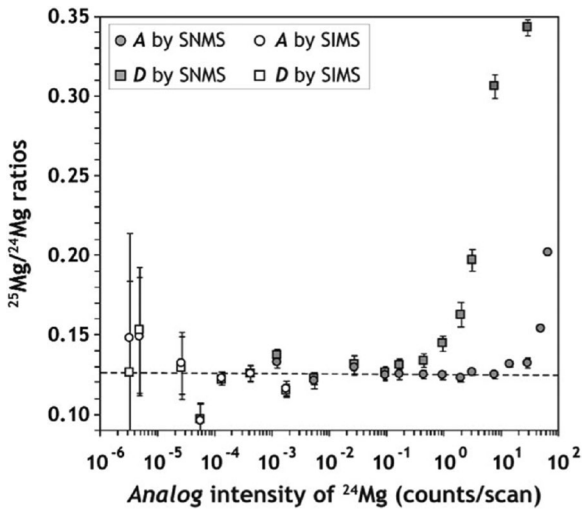

Fig. 9. ^{25}Mg/^{24}Mg intensity ratios as a function of analog intensity of ^{24}Mg. Circle and square symbols denote data points processed by analog and digital modes, respectively. The dotted line represents an average ^{25}Mg/^{24}Mg ratio of analog data by SNMS, excluding data points above 10^1 counts/scan. Adapted from Bajo et al. (2019)

Helium distribution of implanted solar winds

The solar wind directly irradiates the surfaces of airless bodies, such as asteroids, meteorites, and the Moon. The solar wind is composed of hydrogen (~ 95%) and helium (~ 5%). Since the range of the solar wind implanted into solids is several tens of nanometers, the presence of solar wind He is evidence that the solids were exposed on the surfaces of airless bodies. The ^{4}He concentration map of solar wind implantation in the carbonaceous meteorite NWA 801 CR2 is shown in Fig. 11. The meteorite is composed of various minerals ranging in size from nanometers to millimeters. The black areas on the Mg map are mainly composed of fine-grained minerals. Coarse-grained minerals are shown as gray to white areas on the Mg map, depending on the mineral species. The coarse-grained mineral located at site A are rimmed by a ^{4}He layer on its surface. In contrast, the coarse-grained

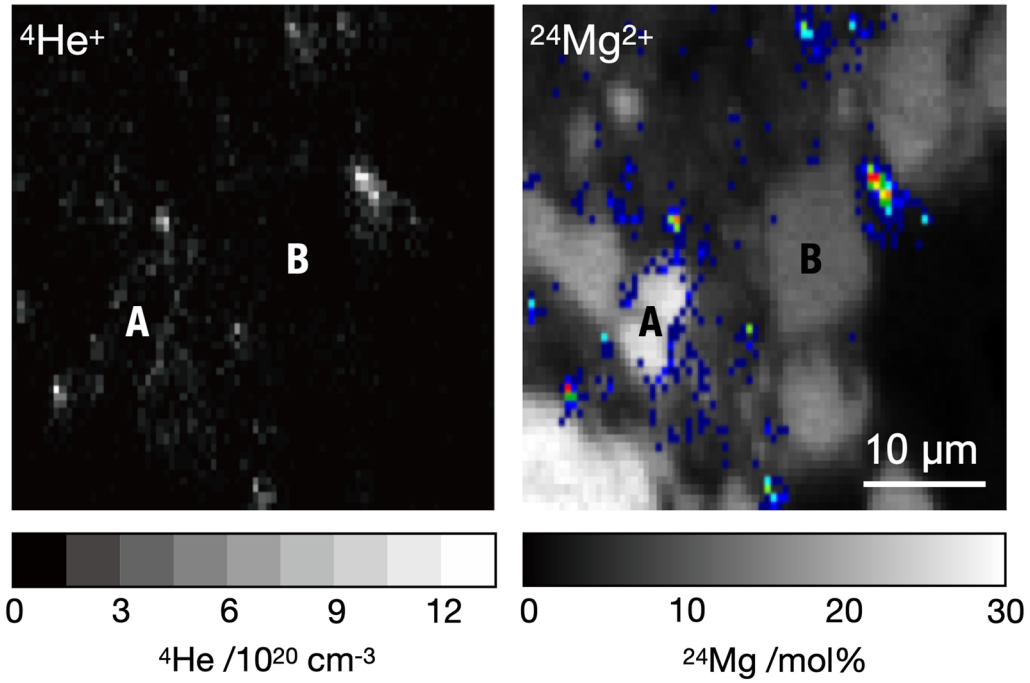

Fig. 11 Quantitative element maps of $^{4}He^{+}$ (left) and $^{24}Mg^{+}$ (right) of NWA 801 CR2 meteorite. Colored dots in the Mg map correspond to ^{4}He distribution shown in the He map. A: grain A (olivine), B: grain B (pyroxene)

mineral located at site B has no ^{4}He layer. This suggests that grain A were exposed on the surface of the parent body and irradiated by the solar wind, whereas grain B had not. The greater number of coarse-grained minerals without ^{4}He rims indicates that most of the coarse-grained minerals were shielded from solar wind beneath the surface. Similarly, the fine-grained minerals concentrated in ^{4}He are scattered among the ^{4}He-free fine-grained minerals. The fine-grained minerals concentrated in ^{4}He were exposed on the surface of the parent body. The proportion of ^{4}He-free fine-grained minerals is greater than that of ^{4}He-enriched. The observed texture suggests that materials exposed on the surface of the parent body have slipped into the interior, probably due to vibration from impact shocks during the accretion of the parent body.

The implantation structure of solar wind ^{4}He in a coarse-grained mineral was studied using the asteroid Itokawa sample returned by the Hayabusa spacecraft (Yurimoto et al. 2011). The Itokawa samples are regolith materials irradiated by the solar wind (Nagao et al. 2011). The three-dimensional analysis with spatial resolutions of 1 μm in lateral (x, y) and 10 nm in depth (z) is shown in Fig. 12. There is a ^{4}He-enriched layer at a depth of ~ 50 nm, suggesting an impact speed of ~ 500 km s^{-1}. This speed is in agreement with the current solar wind speed. In addition, significant heterogeneous distributions parallel to the surface are observed in the He-enriched layer. Yurimoto et al. (2016) showed that He implanted into a substrate beyond the retention limit degasses, while the overall shape of the depth profile is preserved. Therefore, the lateral micrometer-scale heterogeneity in the ^{4}He-enriched layer corresponds to the degassing that occurred in the Itokawa sample. This degassing explanation is supported by studies of the $^{4}He/^{20}Ne$ ratio (Nagao et al. 2011), which ratio decreases with the degassing of noble gases from meteorites because He is degassed faster than Ne. Therefore, a three-dimensional analysis with nanometer-to-micrometer resolution is important to assess how much of the elements implanted by the solar wind remain in the sample in their original state.

Conclusions and future perspective

The development of isotope imaging using LIMAS is reviewed. LIMAS is an SNMS instrument that uses a fs laser to post-ionize neutrals sputtered by Ga ions generated from the LMIS. Using aberration-corrected optics, the primary Ga beam is focused onto the sample surface to a minimum diameter of approximately 10 nm. Since the fs laser ionizes almost all the neutrals in the laser beam via a strong-field ionization mechanism, the matrix effects on element quantification can be greatly reduced. Isobars smaller than $\Delta M/M = 10^{-6}$ can be separated from

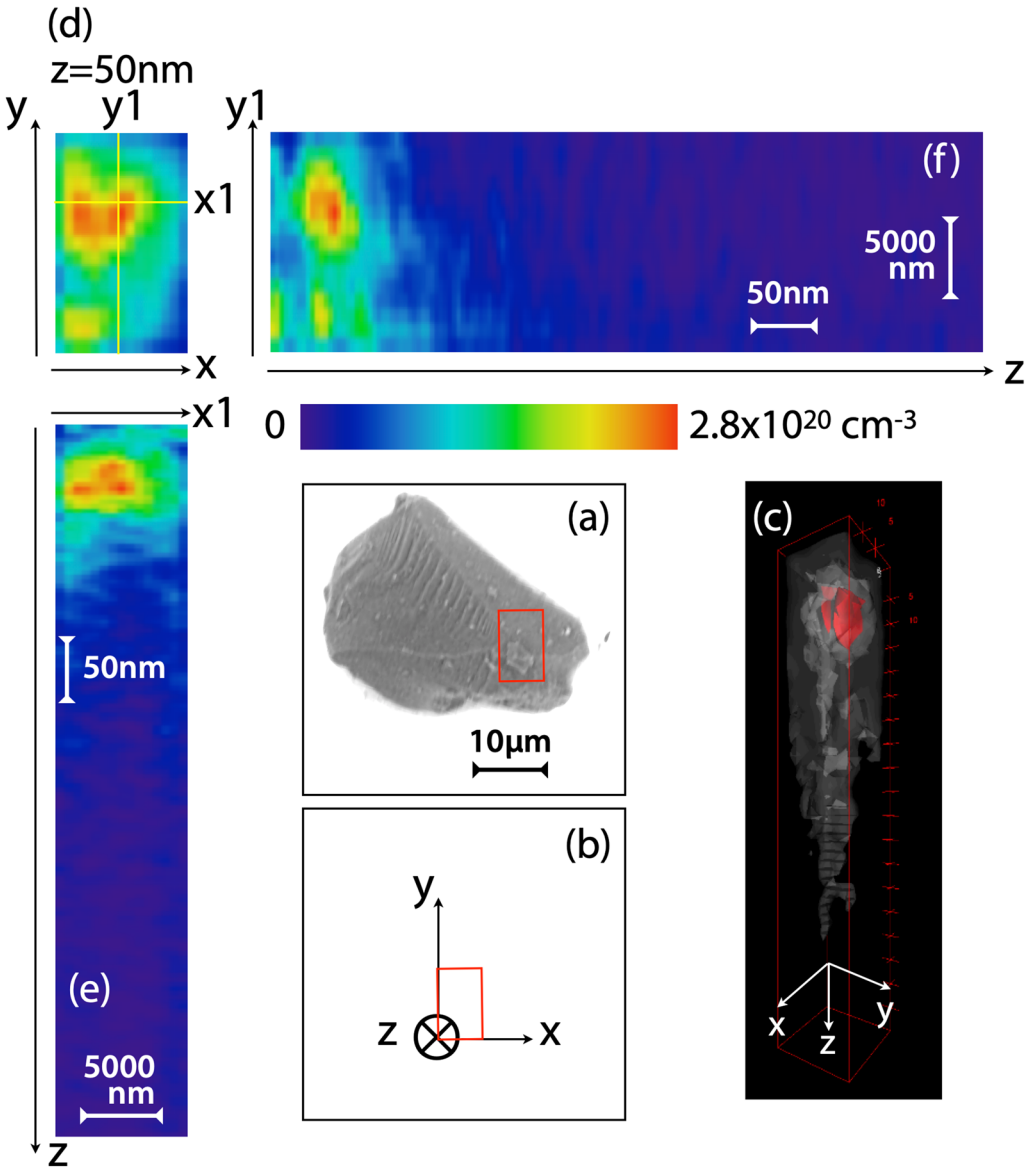

Fig. 12 Solar wind ^{4}He distribution of asteroid Itokawa sample grain, RA-QD02-0169; olivine. **a** Backscattered electron image of the Itokawa sample. Red square: ^{4}He mapping area. **b** *x*–*y*–*z* directions of the ^{4}He mapping area. *x*, *y*: parallel to the surface, z: depth. **c** Three-dimensional map of ^{4}He distribution. Color contours of red color: 10^{20} He cm^{-3}, light gray color: 5×10^{19} He cm^{-3}, and dark gray color: 10^{19} He cm^{-3}. Cuboid size: (*x*, *y*, *z*) = (8 μm, 13 μm, 525 nm). **d** ^{4}He distribution of *x*–*y* plane at z = 50 nm, **e** He distribution of the *x*–*z* cross-section at the line *x*1 shown in (**d**). **f** ^{4}He distribution of the *y*–*z* cross-section at the line y1 shown in (**d**). Color contours of (**d**), (**e**), and (**f**) are shown in the figure

the target isotope peak. The dynamic range of ion detection is ~ 10^9. With these capabilities, the quantification of He in solids can be achieved at concentrations as low as ~ 10^{-3} cm^3 STP g^{-1} (~ 10^{17} cm^{-3}, ~ 1 ppma) with lateral micrometer resolution.

Helium isotope imaging was first realized by LIMAS. The two-dimensional micro-distribution of ^{4}He in a meteorite was determined. The heterogeneous distribution shows that the He is implanted by the solar wind and indicates that surface layer overturns have occurred on the meteorite parent body. The three-dimensional nano-distribution of ^{4}He in the asteroid Itokawa grain has been determined. The distribution shows that the solar wind irradiating Itokawa was similar to the current solar wind. The degassing state of the implanted solar wind ^{4}He can be deduced from the heterogeneous distribution.

Thanks to its high sensitivity, low background, high mass resolution, and high spatial resolution, the LIMAS

instrument has the potential to analyze all trace elements, including Ne and other noble gases, even in the nanometer range in solids.

Abbreviations

SIMS	Secondary ion mass spectrometry
SNMS	Secondary neutral mass spectrometry
LIMAS	Laser ionization mass nanoscope
LMIS	Liquid metal ion source
TOF	Time-of-flight
MS	Mass spectrometer
MULTUM	Multi-turn TOF mass spectrometer
EF	Electrostatic energy analyzer

Acknowledgements
Not applicable.

Author contributions
KB and HY drafted the manuscript. All the authors have read and approved the final version of the manuscript.

Funding
This work was partially supported by Kaken-hi Grants.

Availability of data and materials
Not applicable.

Declarations

Competing interests
There are no competing interests.

Received: 17 November 2023 Accepted: 12 March 2024
Published online: 02 April 2024

References

Bajo K-i, et al. Electronic data acquisition and operational control system for time-of-flight sputtered neutral mass spectrometer. Surf Interface Anal. 2019;51(1):35–9. https://doi.org/10.1002/sia.6541.
Bajo K-i, et al. High spatial resolution imaging of helium isotope by TOF-SNMS. Surf Interface Anal. 2016;48(11):1190–3. https://doi.org/10.1002/sia.6085.
Bajo K-i, et al. Depth profiling analysis of solar wind helium collected in diamond-like carbon film from Genesis. Geochem J. 2015;49(5):559–66. https://doi.org/10.2343/geochemj.2.0385.
Bogard DD, Johnson P. Trapped noble gases indicate lunar origin for Antarctic Meteorite. Geophys Res Lett. 1983;10(9):801–3. https://doi.org/10.1029/GL010i009p00801.
Ebata S, et al. Development of an ultra-high performance multi-turn TOF-SIMS/SNMS system "MULTUM-SIMS/SNMS." J Am Soc Mass Spectrom. 2013;24(2):222–9. https://doi.org/10.1007/s13361-012-0528-2.
Ebata S, et al. Development of laser ionization mass nanoscope (LIMAS). Surf Interface Anal. 2012;44(6):635–40. https://doi.org/10.1002/sia.4857.
Gnaser H, Oechsner H. Noval detection scheme for the analysis of hydrogen and helium by secondary ion mass spectrometry. Surf Interface Anal. 1991;17(9):646–9. https://doi.org/10.1002/sia.740170906.
Greer J, et al. Atom probe tomography of space-weathered lunar ilmenite grain surfaces. Meteorit Planet Sci. 2020;55(2):426–40. https://doi.org/10.1111/maps.13443.
Heck PR, et al. Interstellar residence times of presolar SiC dust grains from the Murchison carbonaceous meteorite. Astrophys J. 2009;698(2):1155–64. https://doi.org/10.1088/0004-637x/698/2/1155.
Ishihara M, et al. Perfect space and time focusing ion optics for multiturn time of flight mass spectrometers. Int J Mass Spectrom. 2000;197(1–3):179–89. https://doi.org/10.1016/S1387-3806(99)00244-4.
Itose S, et al. An aberration corrected FIB for nano-area mass spectrometry. Microsc Microanal. 2011;17(S2):654–5. https://doi.org/10.1017/S1431927611004144.
Ivanov MY, et al. Anatomy of strong field ionization. J Mod Opt. 2005;52(2–3):165–84. https://doi.org/10.1080/0950034042000275360.
Malherbe J, et al. A new radio frequency plasma oxygen primary ion source on nano secondary ion mass spectrometry for improved lateral resolution and detection of electropositive elements at single cell level. Anal Chem. 2016;88(14):7130–6. https://doi.org/10.1021/acs.analchem.6b01153.
Mibuka R, et al. Characteristics of post-ionization using a femto-second laser. Appl Surf Sci. 2008;255:1595–8. https://doi.org/10.1016/j.apsusc.2008.05.003.
Nagao K, et al. Irradiation history of Itokawa regolith material deduced from noble gases in the Hayabusa samples. Science. 2011;333(6046):1128–31. https://doi.org/10.1126/science.1207785.
Nagata K, et al. Aberration-corrected focused ion beam for time-of-flight secondary neutral mass spectrometry. Appl Phys Express. 2019;12(8): 085005. https://doi.org/10.7567/1882-0786/ab30e4.
Nakamura T, et al. Microdistribution of primordial noble gases in CM chondrites determined by in situ laser microprobe analysis: decipherment of nebular processes. Geochim Cosmochim Acta. 1999;63(2):241–55. https://doi.org/10.1016/S0016-7037(98)00275-0.
Obase T, et al. Water-susceptible primordial noble gas components in less-altered CR chondrites: a possible link to cometary materials. Geochim Cosmochim Acta. 2021;312:75–105. https://doi.org/10.1016/j.gca.2021.08.012.
Okazaki R, et al. Noble-gas-rich chondrules in an enstatite meteorite. Nature. 2001;412(6849):795–8. https://doi.org/10.1038/35090520.
Okumura D, et al. A compact sector-type multi-turn time-of-flight mass spectrometer 'MULTUM II.' Nucl Inst Methods Phys Res A. 2004;519:331–7. https://doi.org/10.1016/j.nima.2003.11.249.
Protopapas M, et al. Atomic physics with super-high intensity lasers. Rep Prog Phys. 1997;60(4):389. https://doi.org/10.1088/0034-4885/60/4/001.
Sumino H, et al. Magmatic processes of Unzen volcano revealed by excess argon distribution in zero-age plagioclase phenocrysts. J Volcanol Geotherm Res. 2008;175(1):189–207. https://doi.org/10.1016/j.jvolgeores.2008.03.027.
Tonotani A, et al. Evaluation of multi-turn time-of-flight mass spectrum of laser ionization mass nanoscope. Surf Interface Anal. 2016;48(11):1122–6. https://doi.org/10.1002/sia.6112.
Yurimoto H, et al. Oxygen isotopic compositions of asteroidal materials returned from Itokawa by the Hayabusa mission. Science. 2011;333(6046):1116–9. https://doi.org/10.1126/science.1207776.
Yurimoto H, et al. Quantitative analysis of helium by post-ionization method using femtosecond laser technique. Surf Interface Anal. 2016;48(11):1181–4. https://doi.org/10.1002/sia.6119.

Publisher's Note